

# Emodin-Conjugated PEGylation of Fe<sub>3</sub>O<sub>4</sub> Nanoparticles for FI/MRI Dual-Modal Imaging and Therapy in Pancreatic Cancer

Shuai Ren 


Lina Song

Ying Tian

Li Zhu

Kai Guo

Huifeng Zhang

Zhongqiu Wang 

Department of Radiology, Jiangsu Province Hospital of Chinese Medicine, Affiliated Hospital of Nanjing University of Chinese Medicine, Nanjing, Jiangsu Province, 210029, People's Republic of China

**Background:** Pancreatic cancer (PC) remains a difficult tumor to diagnose and treat. It is often diagnosed as advanced by reason of the anatomical structure of the deep retroperitoneal layer of the pancreas, lack of typical symptoms and effective screening methods to detect this malignancy, resulting in a low survival rate. Emodin (EMO) is an economical natural product with effective treatment and few side effects of cancer treatment. Magnetic nanoparticles (MNPs) can achieve multiplexed imaging and targeted therapy by loading a wide range of functional materials such as fluorescent dyes and therapeutic agents.

**Purpose:** The purpose of this study was to design and evaluate a multifunctional theranostic nanopatform for PC diagnosis and treatment.

**Methods:** In this study, we successfully developed EMO-loaded, Cy7-functionalized, PEG-coated Fe<sub>3</sub>O<sub>4</sub> (Fe<sub>3</sub>O<sub>4</sub>-PEG-Cy7-EMO). Characteristics including morphology, hydrodynamic size, zeta potentials, stability, and magnetic properties of Fe<sub>3</sub>O<sub>4</sub>-PEG-Cy7-EMO were evaluated. Fluorescence imaging (FI)/magnetic resonance imaging (MRI) and therapeutic treatment were examined in vitro and in vivo.

**Results:** Fe<sub>3</sub>O<sub>4</sub>-PEG-Cy7-EMO nanoparticles had a core size of  $9.9 \pm 1.2$  nm, which showed long-time stability and FI/MRI properties. Bio-transmission electron microscopy (bio-TEM) results showed that Fe<sub>3</sub>O<sub>4</sub>-PEG-Cy7-EMO nanoparticles were endocytosed into BxPC-3 cells, while few were observed in hTERT-HPNE cells. Prussian blue staining also confirmed that BxPC-3 cells have a stronger phagocytic ability as compared to hTERT-HPNE cells. Additionally, Fe<sub>3</sub>O<sub>4</sub>-PEG-Cy7-EMO had a stronger inhibition effect on BxPC-3 cells than Fe<sub>3</sub>O<sub>4</sub>-PEG and EMO. The hemolysis experiment proved that Fe<sub>3</sub>O<sub>4</sub>-PEG-Cy7-EMO can be used in vivo experiments. In vivo analysis demonstrated that Fe<sub>3</sub>O<sub>4</sub>-PEG-Cy7-EMO enabled FI/MRI dual-modal imaging and targeted therapy in pancreatic tumor xenografted mice.

**Conclusion:** Fe<sub>3</sub>O<sub>4</sub>-PEG-Cy7-EMO may serve as a potential theranostic nanopatform for PC.

**Keywords:** pancreatic cancer, emodin, magnetic nanoparticles, passive targeting

## Introduction

Pancreatic cancer (PC) is the fourth leading cause of cancer-related mortality, which has an overall 5-year relative survival rate of 9%.<sup>1</sup> Cancer survival rate has improved since the mid-1970s for most common types of cancer with the exception of PC.<sup>2,3</sup> PC is projected to overtake both breast and colorectal cancer as the second leading cause of cancer-related deaths before 2030.<sup>4</sup> The very low survival rate of PC can be summarized to the lack of early diagnosis and effective management strategies.<sup>5,6</sup> Determination of the most efficient therapeutic strategy for treatment of PC is difficult. Some common options such as chemotherapy, surgery, or

Correspondence: Shuai Ren; Zhongqiu Wang  
Department of Radiology, Jiangsu Province Hospital of Chinese Medicine, Affiliated Hospital of Nanjing University of Chinese Medicine, No. 155 Hanzhong Road, Nanjing, Jiangsu Province, 210029, People's Republic of China  
Email sren001@163.com; zhongqiuwang0815@163.com

radiotherapy are toxic and/or may lead to reoccurrence of tumors.<sup>7</sup> Due to the insidious onset, rapid development, and poor prognosis, PC is a serious threat to human health. Therefore, there is a dire need to diagnose early-stage PC using an effective method, which facilitates in reducing the mortality and improving patient survival rates.

Molecular imaging is a non-invasive, painless and safe method, which offers unique insights into biological process and human body.<sup>8,9</sup> It can be used to both diagnose and treat cancer such as PC.<sup>10,11</sup> Magnetic nanoparticles (MNPs), especially iron oxide-based ones (magnetite  $\text{Fe}_3\text{O}_4$ ) are widely used in cancer theranostics due to their excellent stability, novel magnetic properties and surface chemistry for ligand binding and good biocompatibility.<sup>12–14</sup> Compared to gadolinium-based contrast agents (GBCA), MNPs showed stronger magnetic susceptibility effects, image features, and size- or surface chemistry-dependent pharmacokinetics.<sup>15</sup> It can be used to enhance the signals of T1- and T2-weighted images (T1WI and T2WI) while GBCA only provide contrast effects on T1WI images.<sup>12</sup> By loading a wide range of functional materials such as fluorescent dyes and therapeutic agents, MNPs can achieve multiplexed imaging and targeted therapy.

To increase the biocompatibility, prolong blood circulation and biodistribution of MNPs, some polymers such as polyethylene glycol (PEG) are often used to modify the surface of the MNPs considering its high hydrophilicity and low surface tension.<sup>16,17</sup> Macrophages play a fundamental role in the immune system by engulfing foreign particulates such as MNPs.<sup>18</sup> To reduce the phagocytosis of MNPs in vivo, we successfully presented a facile and simple way to encapsulate MNPs in a PEG-modified phospholipid micelle structure ( $\text{Fe}_3\text{O}_4$ @OA@PEG, also known as  $\text{Fe}_3\text{O}_4$ -PEG) in our previous research.<sup>16</sup> However, only single modality MR imaging was used in our previous study. A multifunctional theranostic nanoplatform, combined with multimodal imaging and therapy, is pivotal to improve the diagnostic accuracy and efficacy of PC.

The enhanced permeation and retention (EPR) effect is one of the most widely used mechanisms for passive targeting of NPs to solid tumors.<sup>19</sup> Briefly, the passively targeted NPs release substantial part of therapeutics to tumor tissue and get accumulated owing to the EPR effect which mediated passive-targeting approach.<sup>20,21</sup> To avail this technology, nanomedicine-based strategies are the

most prominent of therapeutic approaches in cancer treatment.<sup>22,23</sup>

Natural products have been proved to play a key role in suppressing the cancer proliferation via different mechanisms in recent years.<sup>24</sup> Emodin (EMO, 6-methyl-1,3,8-tanthragallol) as a natural product, is a tyrosine kinase II inhibitor that is separated from the genus Rhubarb, Polygonum, Buckthorn and Senna.<sup>25</sup> EMO has been widely used in the treatment of cancer such as colorectal cancer and leukemia.<sup>26,27</sup> Compared to synthetic chemical agents, EMO is an economical natural product with effective treatment and few side effects. Recently, Wang et al reported that EMO sensitizes human PC cells to EGFR inhibitor through suppressing Stat3 signaling pathway.<sup>24</sup> In this study, we conjugated EMO to MNPs with the purpose to increase its solubility and enhance the cellular uptake and antitumor efficacy. We also conjugated Cy7 to MNPs to allow fluorescence imaging (FI).

In this study, we developed a theranostic nanoplatform based on MNPs for PC. The subsequent in vitro experiments proved that the theranostic nanoplatform ( $\text{Fe}_3\text{O}_4$ -PEG-Cy7-EMO) could enable FI/MRI dual-modal imaging and provide therapeutic treatment for PC cells. Then in vivo FI/MRI experiments were done to prove the passive targeting and therapeutic effects of the nanoplatform in pancreatic tumor xenografted mice.

## Materials and Methods

### Materials and Reagents

All reagents were commercially available. MNPs were synthesized by Materials Science and Engineering Laboratory at Southeast University (Nanjing, China). The manufacturer details of the reagents are listed as follows: EMO was purchased from Shanghai YuanYe Biotechnology Ltd (Shanghai, China); Cy7-NHS ester, N-(3-dimethylaminopropyl)-N-ethylcarbodiimide hydrochloride (EDC) and N-hydroxysuccinimide (NHS) were purchased from J&K Chemical Ltd (Shanghai, China). Dimethyl sulfoxide (DMSO), Annexin V-fluorescein isothiocyanate (FITC)/propidium iodide (PI) apoptosis detection agents and Matrigel, 3-(4,5-dimethylthiazol-2-yl)-2,5-diphenyltetrazolium bromide (MTT) were purchased from Sangon Biological Engineering Technology & Services Ltd (Shanghai, China). Bovine serum albumin (BSA) was purchased from Sigma-Aldrich (MO, USA); Human pancreatic cell line BxPC-3 was purchased from the Chinese Academy of Sciences Shanghai Branch Cell Bank (Shanghai, China); The hTERT-HPNE (Human

Pancreatic Nestin Expressing) cell line was purchased from Shanghai BoQianer Biological Science and Technology Ltd (Shanghai, China).

## Preparation of Fe<sub>3</sub>O<sub>4</sub>-PEG

The stable Fe<sub>3</sub>O<sub>4</sub>-PEG solution was prepared by a simple way of stirring and ultrasound to modify the PEG-phospholipid onto the surface of the oleic acid (OA) coated MNPs (Fe<sub>3</sub>O<sub>4</sub>@OA) as we have reported previously.<sup>16,28</sup> In brief, a certain concentration of 15 mg Fe/mL and 30 mg Fe/mL of Fe<sub>3</sub>O<sub>4</sub>@OA chloroform solution was prepared by transferring Fe<sub>3</sub>O<sub>4</sub>@OA MNPs into chloroform. A concentration of 100 mg/mL DSPE-PEG2000 chloroform solution was made by dissolving DSPE-PEG2000 into chloroform. A concentration of 500 mg/mL of soybean oil chloroform solution was also made. Then, a mixture of Fe<sub>3</sub>O<sub>4</sub>@OA chloroform solution, DSPE-PEG2000 chloroform solution, and soybean oil chloroform solution were stirred uniformly, which was then added to 20mL of boiling water dropwise under vigorous stirring (2000 r/min) for 30 min. At last, the reaction mixture was dispersed by the ultrasonication (VCX 750, Sonics, America) after organic solvent evaporation and the solution was cooled to room temperature. The obtained sample was filtered by 220 nm membrane and stored at 4°C.

## Conjugation of Cy7 and EMO to Fe<sub>3</sub>O<sub>4</sub>-PEG

The synthesis of Fe<sub>3</sub>O<sub>4</sub>-PEG-Cy7-EMO was carried out in three steps. First, the carboxylic group of a lysosomal enzyme-sensitive peptide linker (Gly-Phe-Leu-Gly, GFLG) was activated for 20 min via EDC and NHS activation in DMF.<sup>29</sup> Thereafter, EMO was added and reacted for two hours, and then, the carboxylic group of the chosen amino acid was linked to the hydroxyl group of EMO (GFLG-EMO). Second, Fe<sub>3</sub>O<sub>4</sub>-PEG MNPs were dissolved in MES buffer (0.1 M, pH 5); then, 1 mg EDC and 1 mg NHS were added. Third, GFLG-EMO and Cy7 were added to the solution and mixed on a rotary shaker for 12 hours. In the aforementioned steps, GFLG-EMO and Cy7-NHS ester (10 µM) were covalently grafted onto Fe<sub>3</sub>O<sub>4</sub>-PEG based on an esterification reaction between the carboxyl group and the amino group.<sup>18,30</sup> The theranostic nanoparticle Fe<sub>3</sub>O<sub>4</sub>-PEG-Cy7-EMO was finally obtained.

The number of Fe<sub>3</sub>O<sub>4</sub>-PEG-Cy7-EMO nanoparticles and the surface area of Fe<sub>3</sub>O<sub>4</sub>-PEG-Cy7-EMO nanoparticle

were measured and calculated in S1.1 (see [Supplemental Methods](#)). The conjugation efficacy of EMO to Fe<sub>3</sub>O<sub>4</sub>-PEG-Cy7-EMO nanoparticle was measured and calculated in S1.2 (see [Supplemental Methods](#)).

## Characterization of Nanoparticles (NPs)

The morphologies of the NPs were measured using transmission electron microscopy (TEM, Joel, JEM-1011, Japan). The magnetic properties of NPs were measured using vibrating sample magnetometer (VSM, Lakeshore 7407, USA) with a saturating field of 1.0 Tesla. The sample of the Fe<sub>3</sub>O<sub>4</sub>-PEG was characterized using Fourier transform infrared (FTIR, Thermo Nicolet AVATAR 360 FTIR, America) using 5 mg of sample. The hydrodynamic size of NPs was measured using dynamic light scattering (DLS, Malvern Panalytical). The zeta potentials of NPs were measured using Zeta-Plus analyzer (Brookhaven Instruments Co., NY, USA). The stability of NPs in sodium chloride (NaCl, 0 to 1.0 mM) solution containing 5% BSA and in different pH (3 to 11) solution was observed for 7 days.

## In vitro Multimodal Imaging

The T2 relaxation of NPs at different Fe concentrations was measured using a 1.5 T MR system (MAGNETOM Aera, Siemens, Germany). The scanning parameters were as follows: repetition time (TR) 2500 ms; echo time (TE) 22 ms; flip angle 120 deg; slices 30 (Dist. factor 10%); Field of view (FOV) read 230 mm; FOV phase 87.5%; base resolution 512; phase resolution 60%; slice thickness 4 mm; averages 1. The fluorescence emission spectrums of NPs at different Fe concentrations were measured using Caliper IVIS SpectrumCT In Vivo Imaging System (PerkinElmer, MA, USA) with a detection excitation wavelength at 750 nm and emission wavelength at 788 nm.

## Cellular Uptake of NPs via TEM and Prussian Blue Staining

The cellular uptake of NPs in vitro was evaluated using a bio-TEM (Tecnai G2 Polara; FEI, Hillsboro, USA). BxPC-3 and hTERT-HPNE cells were first seeded in six-well plates in RPMI-1640 or DMEM medium supplemented with 10% FBS and 1% penicillin-streptomycin at 37°C and 5% CO<sub>2</sub> for 24 hours for cell attachment. Next, we changed the medium with fresh medium containing 40µg/mL Fe<sub>3</sub>O<sub>4</sub>-PEG-Cy7-EMO and incubated at 37°C for 6

hours. After being labeled, the cells were washed with distilled water and collected, and then fixed with 2.5% glutaraldehyde at room temperature for 1 hour. The samples were dehydrated with ethanol and embedded in propylene oxide and prepared for observation under the bio-TEM.

Perl's Prussian blue staining was carried out to visualize the cellular uptake of NPs under an optical microscopy (Olympus CKX41, Tokyo, Japan).<sup>31</sup> After being labeled, the BxPC-3 and hTERT-HPNE cells were washed three times with PBS and fixed in 4% paraformaldehyde solution for 20 min. Finally, the cells were stained with 4% potassium ferrocyanide in 10% hydrogen chloride (HCl) for 30 min at room temperature and counterstained with nuclear fast red.

## Cell Viability Assay and Apoptosis Analyses

The effect of Fe<sub>3</sub>O<sub>4</sub>-PEG and Fe<sub>3</sub>O<sub>4</sub>-PEG-Cy7-EMO on BxPC-3 cells was determined using cell viability analysis by the MTT assay (Roche Diagnostics, Mannheim, Germany), using hTERT-HPNE cell line as control group. The BxPC-3 and hTERT-HPNE cells were seeded in 96-well plates at  $5 \times 10^3$  per well in RPMI-1640 or DMEM medium and incubated at 37°C and 5% CO<sub>2</sub> for cell attachment. Next, different concentrations of Fe<sub>3</sub>O<sub>4</sub>-PEG and Fe<sub>3</sub>O<sub>4</sub>-PEG-Cy7-EMO (0, 12.5, 25, 50, 80, 100 µg/mL) were added to the plates and incubated for 24 hours. Thereafter, the previous medium was removed and 50 µL of MTT dye solution was added to each well and incubated for 4 hours. Finally, 150 µL of dimethyl sulfoxide was added to each well and vibrated in the plate shake under dark condition. Optical density (OD) values were recorded at 490 and 570 nm on a microplate reader (model 680, Bio-RAD, USA). The percentage of inhibition of NPs was calculated as inhibition (%) = (OD control – OD sample)/OD control × 100%.<sup>32</sup> Subsequently, IC<sub>50</sub> (the concentration at which a substance exerts half of its maximal inhibitory effect) was determined by the regression curve of cell viability.

Flow cytometry assays were done to quantitatively analyze NPs-induced apoptosis or necrosis. First, BxPC-3 and hTERT-HPNE cells were seeded in six-well plates at  $1 \times 10^6$  per well and incubated for 24 hours for cell attachment. Next, the previous medium was replaced with fresh medium containing different concentrations of NPs (0, 40, and 80 µg/mL) for 24 hours. After incubation with NPs, the cells were collected and then resuspended in PBS and

stained with Annexin V-FITC/PI. The fluorescence signals of samples were obtained by a flow cytometric analyzer (BD Biosciences).

## In vitro Hemocompatibility Testing of NPs

The hemolysis experiment was performed to examine the hemolytic properties of NPs.<sup>33,34</sup> About 5 mL heart blood from Sprague Dawley Rats was collected into the Erlenmeyer flask containing glass beads. About 10 times the amount of sterile 0.9% NaCl saline was added to the flask and shook, then centrifuged at 1500 rpm for 10 min. After removing the supernatant, the sedimented red blood cells (RBC) were washed with saline 2–3 times until the supernatant was clear. Two percent of RBC suspension was made of red cells and sterile saline. Sterile saline, distilled water, 2% RBC suspension and NPs (1mg/mL Fe<sub>3</sub>O<sub>4</sub>-PEG and 1mg/mL Fe<sub>3</sub>O<sub>4</sub>-PEG-Cy7-EMO) were added to five tubes according to [Supplementary Table 1](#). Thereafter, the tubes were placed under room temperature for incubation. The hemolysis phenomenon was observed at different time points from 15 min, 30 min, 45 min, 1 hour, 2 hours, and 4 hours. The 4th tube with 2.5mL 2% RBC suspension and 2.5mL sterile saline and the 5th tube with 2.5mL 2% RBC suspension and 2.5mL distilled water were set as the negative and positive groups. Ultraviolet spectrophotometry was adopted to measure the OD values and hemolysis rates (HRs) of the supernatant for each group according to the following formula:  $HR = (OD_{C0} - OD_{C1}) / (OD_{C2} - OD_{C1}) \times 100\%$ ; OD<sub>C0</sub>, OD<sub>C1</sub>, and OD<sub>C2</sub> represented the OD values of NPs, negative group, and positive group.

## Orthotopic Human Pancreatic Tumor Xenograft Model

All animal experiments were performed in compliance with the ethical guidelines established by the local animal care authorities at Affiliated Hospital of Nanjing University of Chinese Medicine (2019 DW-19-02). Healthy athymic BALB/C male nude mice, 4 weeks old, weighting 18–22g, were purchased from Changzhou Cavens Experimental Animal Ltd (Changzhou, China) as we previously reported.<sup>6</sup> They were raised under pathogen-free conditions and kept at a temperature of 25°C following a standard light/dark cycle. The orthotopic pancreatic tumor xenograft model was established by injecting an amount of  $5 \times 10^5$  BxPC-3-GFP cells subcutaneously into the right flanks of the mice. The tumor was harvested



and cut into  $1\text{mm}^3$  fragments when it reached 7–10 mm in diameter. Then the tumor fragment was implanted into the pancreas of the nude mice with the help of surgical orthotopic transplantation.<sup>35</sup> Finally, the mice were used for further analysis when the pancreatic tumor reached 5–10 mm in diameter.

## In vivo MRI, FI, and Histological Analysis

The multimodal imaging properties of  $\text{Fe}_3\text{O}_4$ -PEG and  $\text{Fe}_3\text{O}_4$ -PEG-Cy7-EMO in vivo were evaluated using 12 BxPC-3 orthotopic pancreatic tumor mice. Twelve mice were divided into two groups, one group was injected with an amount of 0.2mL–0.4mL  $\text{Fe}_3\text{O}_4$ -PEG or  $\text{Fe}_3\text{O}_4$ -PEG-Cy7-EMO for FI and the other group was injected with an amount of 0.2mL–0.4mL  $\text{Fe}_3\text{O}_4$ -PEG or  $\text{Fe}_3\text{O}_4$ -PEG-Cy7-EMO for MR imaging.

For MR imaging, a rodent receiver coil (Chenguang Medical Technologies Ltd, Shanghai, China) and 3.0 T MRI scanner (Siemens MAGNETOM Verio, Germany) were used. First, axial unenhanced T2WI sequence was obtained prior to NPs injection. After that, different scanning time points including 2, 4, 6, 24 and 48 h were obtained after NPs injection and time intensity curves (TICs) on T2WI images were generated by placing a circular ROI on the tumor region. The scan parameters for T2WI were as following: TR: 4000 ms; TE: 84 ms; Flip angle: 120 deg; Slices: 17 (Dist. factor 10%); Fov read: 78 mm; Fov phase: 77.5%; Base resolution: 320; Phase resolution: 100%; Slice thickness: 0.9 mm; Averages: 2. After imaging, one mouse in each group was sacrificed at the predetermined time points (6, 24, and 48 h) after tail vein injection.

For FI, Caliper IVIS SpectrumCT In Vivo Imaging System (PerkinElmer, MA, USA) was adopted with the following parameters (excitation wavelength: 750 nm, emission wavelength: 788 nm, and exposure time: 0.1 s). FI was obtained before and after tail vein injection (2, 4, 6, 24 and 48 h). After imaging, one mouse in each group was sacrificed at the predetermined time points (6, 24 and 48 h) after tail vein injection.

Pancreatic tumors and normal tissues including hearts, livers, spleens, lungs, and kidneys were collected from the sacrificing mice, and then fixed in 4% formaldehyde solution for 24 h at 4°C, embedded in paraffin and cut into 4- $\mu\text{m}$ -thick sections. Histological analysis was performed by hematoxylin and eosin (H&E) staining to assess the cellular and morphological structures.<sup>36</sup> Additionally,

Prussian blue staining was performed in order to detect iron NPs accumulated in tumors or tissues.<sup>37,38</sup>

## In vivo Antitumor Efficacy

The in vivo antitumor efficacy of  $\text{Fe}_3\text{O}_4$ -PEG-Cy7-EMO was examined using 12 orthotopic human pancreatic tumor xenograft models, using  $\text{Fe}_3\text{O}_4$ -PEG, EMO, and sterile saline as control groups. The mean body weight and mean tumor volume of mice in different treatment groups were recorded. On the last day, the tumors were harvested for observation of the antitumor effect of the NPs and control groups.

## Statistical Analysis

Quantitative variables were presented as mean  $\pm$  SD and were analyzed using the Student's *t*-test or Mann–Whitney test. Statistical significance was defined as  $P < 0.05$ . All analyses were carried out using SPSS (version 22.0 IBM Corp.). Dose-dependent inhibition rates of different treatment groups, TICs representing the average signal intensities versus different concentrations of NPs in vivo on T2WI imaging, and time-dependent tumor volume and body weight of mice were obtained using 64-bit OriginPro 8.6.

## Results

### Synthesis and Characterization of NPs

The synthesis of  $\text{Fe}_3\text{O}_4$ -PEG-Cy7-EMO is shown in Figure 1A. The possible mechanism of  $\text{Fe}_3\text{O}_4$ -PEG-Cy7-EMO enabled FI/MRI dual-modal imaging and targeted therapy in pancreatic tumor xenografted mice based on the EPR effect is shown in Figure 1B.

The characterizations of the NPs are shown in Figure 2. Figure 2A shows that the  $\text{Fe}_3\text{O}_4$ -PEG had a nearly spherical shape and excellent dispersity with a core size of  $9.1 \pm 1.7$  nm. The TEM image of  $\text{Fe}_3\text{O}_4$ -PEG-Cy7-EMO is shown in Figure 2B, which has a core size of  $9.9 \pm 1.2$  nm. Figure 2C shows that  $\text{Fe}_3\text{O}_4$ -PEG-Cy7-EMO has the characteristics of superparamagnetic property at room temperature. FTIR of  $\text{Fe}_3\text{O}_4$ -PEG (5mg sample) is shown in Figure 2D. Figure 2E shows that the hydrodynamic size of  $\text{Fe}_3\text{O}_4$ -PEG and  $\text{Fe}_3\text{O}_4$ -PEG-Cy7-EMO are  $26.12 \pm 5.13$  nm and  $27.16 \pm 5.74$  nm; Additionally, little changes of hydrodynamic sizes of  $\text{Fe}_3\text{O}_4$ -PEG-Cy7-EMO were observed in different pH buffer solutions (Figure 2F). The zeta potentials of  $\text{Fe}_3\text{O}_4$ -PEG (Figure 2G) and  $\text{Fe}_3\text{O}_4$ -PEG-Cy7-EMO

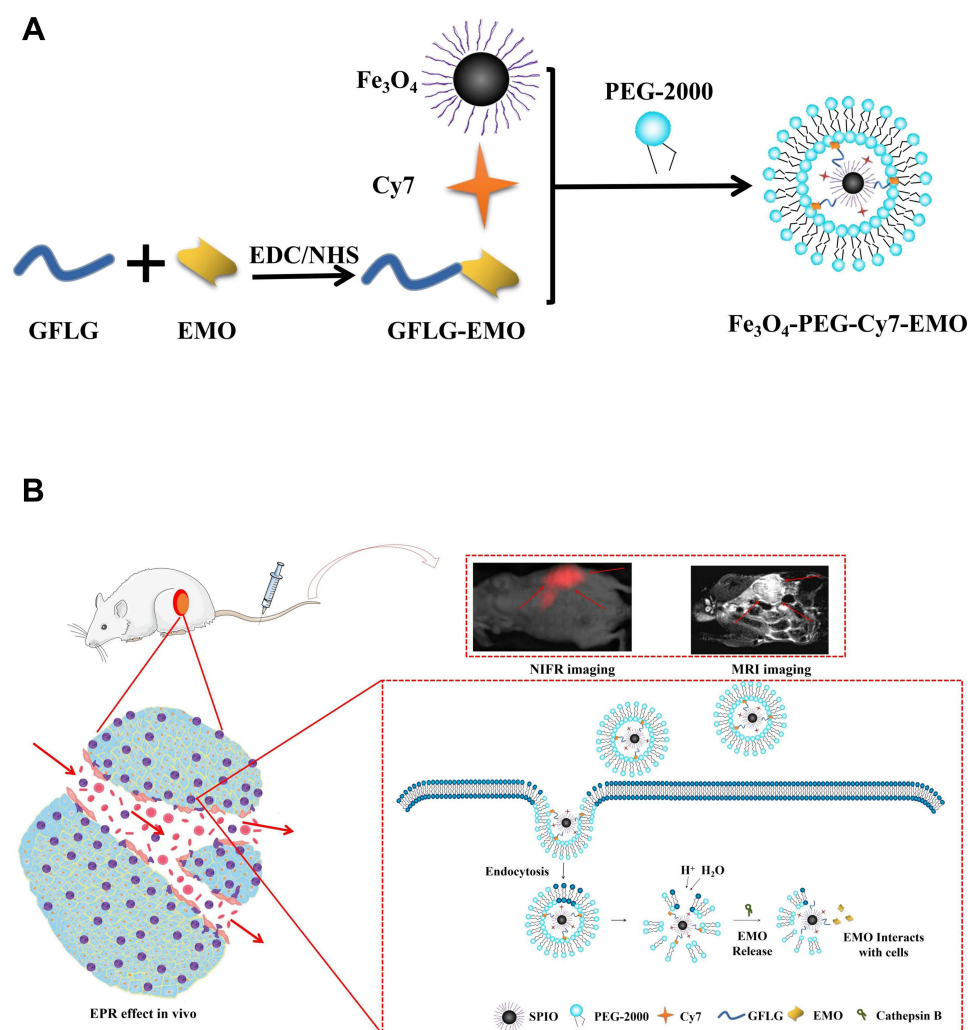


**Figure 1** Schematic illustration of the synthesis of  $\text{Fe}_3\text{O}_4$ -PEG-Cy7-EMO (**A**) and the possible mechanism of  $\text{Fe}_3\text{O}_4$ -PEG-Cy7-EMO enabled FI/MRI dual-modal imaging and targeted therapy in pancreatic tumor xenografted mice based on the EPR effect (**B**).

**Abbreviations:** EMO, emodin; GFLG, Gly-Phe-Leu-Gly; PEG, polyethylene glycol; EDC, N-(3-dimethylaminopropyl)-N-ethylcarbodiimide hydrochloride; NHS, N-hydroxysuccinimide; EPR, enhanced permeation and retention.

(Figure 2H) are  $-40.2 \pm 6.83$  mV and  $-38.7 \pm 6.32$  mV; Additionally, little changes of zeta potentials of  $\text{Fe}_3\text{O}_4$ -PEG-Cy7-EMO were observed in different pH buffer solutions (Figure 2I). The stability of  $\text{Fe}_3\text{O}_4$ -PEG-Cy7-EMO in sodium chloride (0 to 1.0 mM) solution (containing 5% BSA) and in different pH (3 to 11, Figure 2K) solution was observed for 7 days (Figure 2J and K). No deposition is observed in  $\text{Fe}_3\text{O}_4$ -PEG-Cy7-EMO solutions that were stored at  $4^\circ\text{C}$  for 7 days.

The number of  $\text{Fe}_3\text{O}_4$ -PEG-Cy7-EMO nanoparticles and the surface area of  $\text{Fe}_3\text{O}_4$ -PEG-Cy7-EMO nanoparticle were measured and calculated in S2.1 (see Supplemental Results). The conjugation efficacy of EMO to  $\text{Fe}_3\text{O}_4$ -PEG-Cy7-EMO nanoparticle was measured and calculated in S2.2 (see Supplemental Results).

## In vitro Multimodal Imaging

Figure 3A shows Fe concentration-dependent T2WI intensity. The T2WI intensity signals decreased with the increase of Fe concentrations. The NPs can shorten T2 relaxation time with  $r^2$  value of  $95.0 \text{ mM}^{-1} \cdot \text{S}^{-1}$  for  $\text{Fe}_3\text{O}_4$ -PEG and  $103.5 \text{ mM}^{-1} \cdot \text{S}^{-1}$  for  $\text{Fe}_3\text{O}_4$ -PEG-Cy7-EMO. Figure 3B demonstrates that the fluorescence intensity decreased with the decrease of the concentrations of  $\text{Fe}_3\text{O}_4$ -PEG-Cy7-EMO, which was proved to be a potential fluorescence imaging contrast agent.

## Cellular Uptake of NPs

We evaluated the cellular uptake of  $\text{Fe}_3\text{O}_4$ -PEG-Cy7-EMO in BxPC-3 and hTERT-HPNE cells using a bio-TEM. At

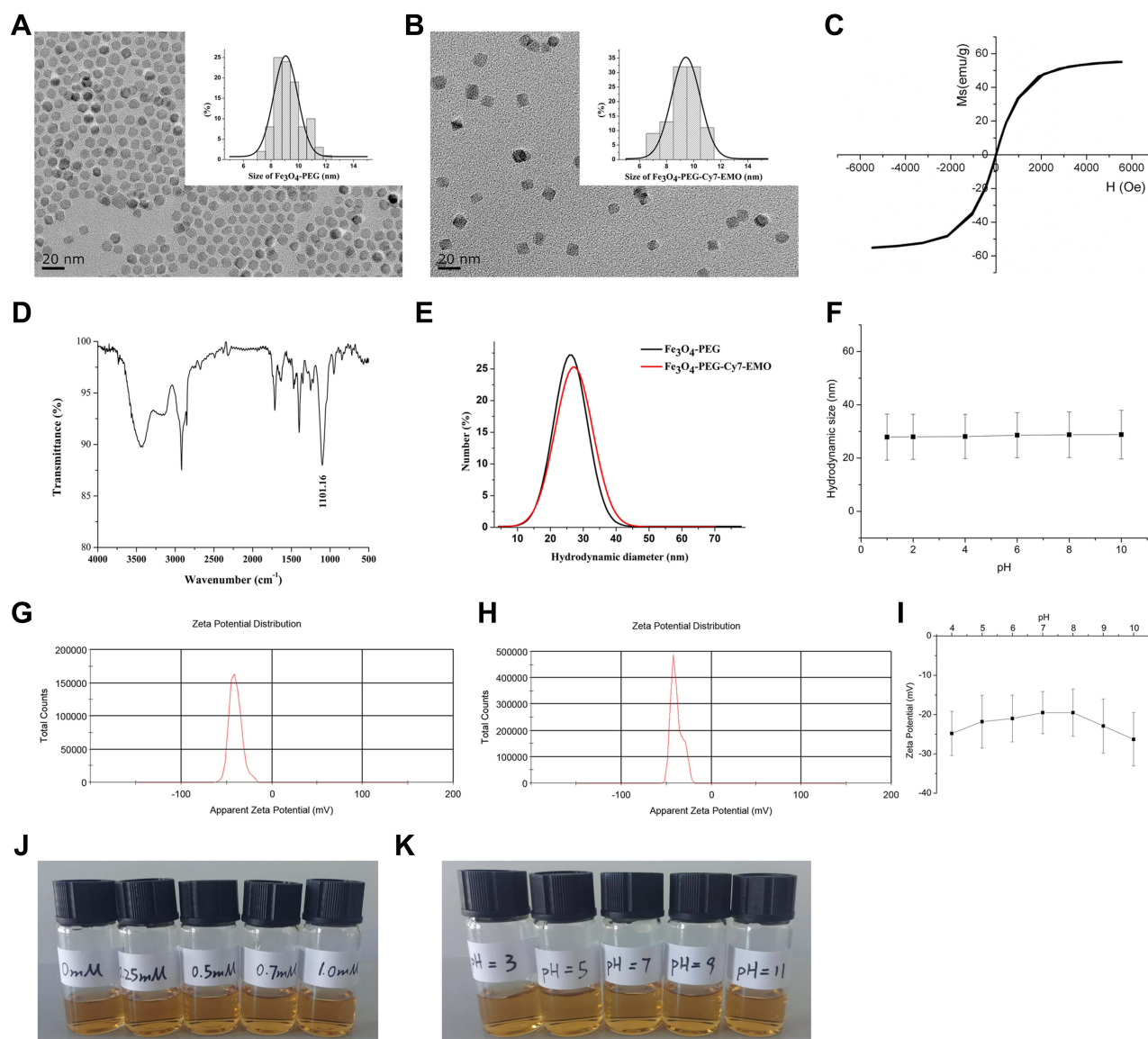


**Figure 2** Characterization of NPs.

**Notes:** (A) TEM image of  $\text{Fe}_3\text{O}_4$ -PEG, which has a core size of  $9.1 \pm 1.7$  nm. (B) TEM image of  $\text{Fe}_3\text{O}_4$ -PEG-Cy7-EMO, which has a core size of  $9.9 \pm 1.2$  nm. (C) The hysteresis curve shows that  $\text{Fe}_3\text{O}_4$ -PEG-Cy7-EMO has the characteristics of superparamagnetic property at room temperature. (D) FT-IR of  $\text{Fe}_3\text{O}_4$ -PEG ( $1101.16 \text{ cm}^{-1}$  C-O-C group). (E) The hydrodynamic size of  $\text{Fe}_3\text{O}_4$ -PEG ( $26.12 \pm 5.13$  nm) and  $\text{Fe}_3\text{O}_4$ -PEG-Cy7-EMO ( $27.16 \pm 5.74$  nm) was characterized by dynamic light scattering (DLS). (F) Hydrodynamic size distributions of  $\text{Fe}_3\text{O}_4$ -PEG-Cy7-EMO in different pH buffer solutions. (G) The zeta potential of  $\text{Fe}_3\text{O}_4$ -PEG ( $-40.2 \pm 6.83$  mV). (H) The zeta potential of  $\text{Fe}_3\text{O}_4$ -PEG-Cy7-EMO ( $-38.7 \pm 6.32$  mV). (I) Zeta potential distributions of  $\text{Fe}_3\text{O}_4$ -PEG-Cy7-EMO in different pH buffer solutions. (J and K) The stability of  $\text{Fe}_3\text{O}_4$ -PEG-Cy7-EMO in sodium chloride (0 to 1.0 mM, Figure 2J) solution (containing 5% BSA) and in different pH (3 to 11, Figure 2K) solution was observed for 7 days. No deposition is observed in  $\text{Fe}_3\text{O}_4$ -PEG-Cy7-EMO solutions that were stored at  $4^\circ\text{C}$  for 7 days.

higher magnification (200 nm), a higher frequency of  $\text{Fe}_3\text{O}_4$ -PEG-Cy7-EMO NPs were observed in BxPC-3 cells than in hTERT-HPNE cells after incubation with  $\text{Fe}_3\text{O}_4$ -PEG-Cy7-EMO NPs for 6 hours; Notably, the NPs were trapped in lysosomes and endosomes (red arrows, Figure 4A). These results suggest that BxPC-3

cells have a stronger phagocytic ability compared to hTERT-HPNE cells.

Subsequently, the accumulation of  $\text{Fe}_3\text{O}_4$ -PEG-Cy7-EMO in PC cells was also confirmed by Prussian Blue staining. A higher frequency of iron positive cells was detected in BxPC-3 cells than in hTERT-HPNE cells

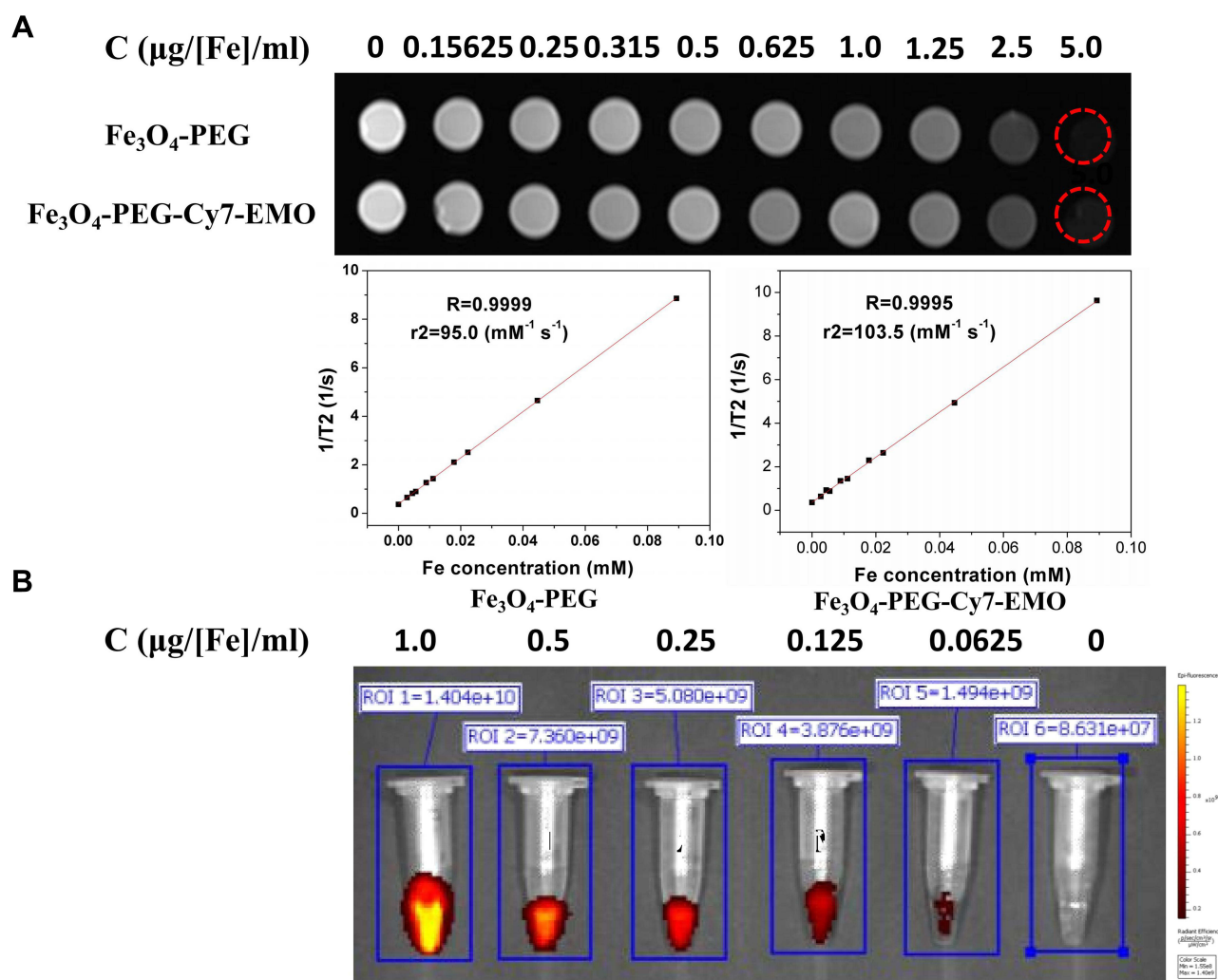


**Figure 3** Fe<sub>3</sub>O<sub>4</sub>-PEG-Cy7-EMO enabled FI/MRI dual-modal imaging in vitro.

**Notes:** (A) T2-weighted MR imaging of Fe<sub>3</sub>O<sub>4</sub>-PEG and Fe<sub>3</sub>O<sub>4</sub>-PEG-Cy7-EMO in vitro. The T2 signal intensities decrease with the increase of the concentration of Fe. (B) Fluorescence imaging of Fe<sub>3</sub>O<sub>4</sub>-PEG-Cy7-EMO in vitro. The fluorescence intensities increase with the increase of the concentration of Fe<sub>3</sub>O<sub>4</sub>-PEG-Cy7-EMO.

after incubation with Fe<sub>3</sub>O<sub>4</sub>-PEG-Cy7-EMO NPs (Figure 4B). These results were in accordance with the TEM results in vitro.

## Cell Viability Assay and Flow Cytometry Analysis

MTT was adopted to test the cytotoxicity of Fe<sub>3</sub>O<sub>4</sub>-PEG, Fe<sub>3</sub>O<sub>4</sub>-PEG-Cy7-EMO and EMO in BxPC-3 and hTERT-HPNE cells. Fe<sub>3</sub>O<sub>4</sub>-PEG-Cy7-EMO had a stronger cytotoxicity for BxPC-3 cells compared to Fe<sub>3</sub>O<sub>4</sub>-PEG (Figure 5A). Similar results were found in BxPC-3 cells treated with Fe<sub>3</sub>O<sub>4</sub>-PEG-Cy7-EMO and EMO, where the former had a stronger cytotoxicity than the latter (Figure 5A). Both Fe<sub>3</sub>O<sub>4</sub>-PEG and Fe<sub>3</sub>O<sub>4</sub>-PEG-Cy7-EMO showed less inhibition against hTERT-HPNE cells, which may be explained by

the fact that BxPC-3 cells have a stronger phagocytic ability of NPs compared to hTERT-HPNE cells. Statistical significances of IC<sub>50</sub> were observed in BxPC-3 cells incubated with Fe<sub>3</sub>O<sub>4</sub>-PEG, EMO, and Fe<sub>3</sub>O<sub>4</sub>-PEG-Cy7-EMO (415.19 ± 13.86 μg/mL vs 56.36 ± 2.28 μg/mL,  $P < 0.001$ ; 415.19 ± 13.86 μg/mL vs 27.30 ± 1.64 μg/mL,  $P < 0.001$ ; 56.36 ± 2.28 μg/mL vs 27.30 ± 1.64 μg/mL,  $P < 0.001$ ); Similar results were observed in hTERT-HPNE cells incubated with Fe<sub>3</sub>O<sub>4</sub>-PEG, EMO, and Fe<sub>3</sub>O<sub>4</sub>-PEG-Cy7-EMO (32653.07 ± 673.38 μg/mL vs 104.53 ± 8.12 μg/mL,  $P < 0.001$ ; 32653.07 ± 673.38 μg/mL vs 87.11 ± 4.75 μg/mL,  $P < 0.001$ ; 104.53 ± 8.12 μg/mL vs 87.11 ± 4.75 μg/mL,  $P = 0.033$ ).

Additionally, we also performed flow cytometry assay to examine the apoptotic rates of NPs, where Fe<sub>3</sub>O<sub>4</sub>-PEG-Cy7-EMO group had a stronger apoptotic rate on cells than Fe<sub>3</sub>O<sub>4</sub>-PEG group (Figure 5B). In brief, Fe<sub>3</sub>O<sub>4</sub>-PEG-Cy7-EMO



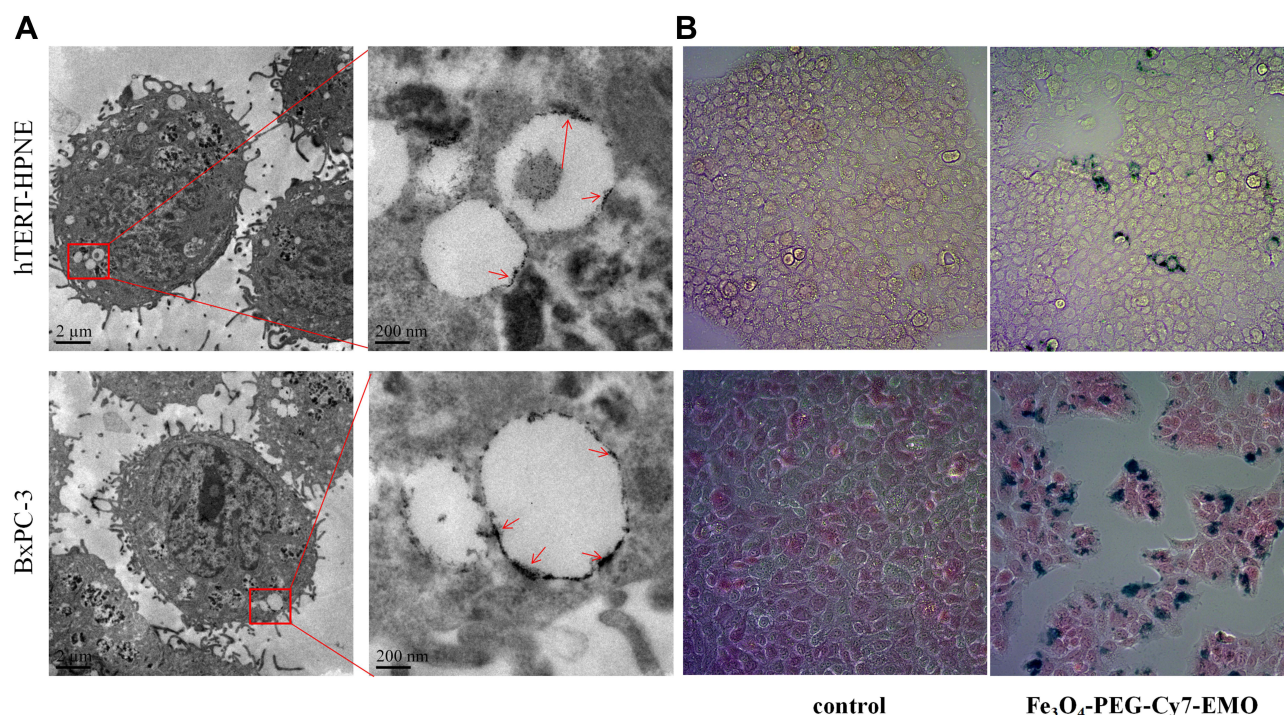


**Figure 4** (A) The distribution of Fe<sub>3</sub>O<sub>4</sub>-PEG-Cy7-EMO in BxPC-3 and hTERT-HPNE cells examined by bio-TEM under 2 μm and 200 nm scale bars. (B) The distribution of Fe<sub>3</sub>O<sub>4</sub>-PEG-Cy7-EMO in BxPC-3 and hTERT-HPNE cells examined by Prussian Blue staining analysis.

NPs had a stronger inhibition effect on BxPC-3 cells than on hTERT-HPNE cells, which was consistent with MTT results. The cell apoptotic rates of different NPs in BxPC-3 and hTERT-HPNE cells are shown in Table 1.

### In vitro Hemocompatibility Testing of NPs

The hemolysis experiment was performed to examine the hemolytic properties of NPs. The hemolysis phenomenon and hemolysis rates are shown in Figure 6A and B. These results showed that Fe<sub>3</sub>O<sub>4</sub>-PEG and Fe<sub>3</sub>O<sub>4</sub>-PEG-Cy7-EMO NPs have a good hemocompatibility, which can be used for further in vivo analysis.

### In vitro FI/MRI, Histological and Prussian Blue Staining Analysis

We validated the multimodal imaging effects of NPs in vivo using FI/MRI, histological and Prussian Blue staining analysis. First, we observed the time-dependent biodistribution of Fe<sub>3</sub>O<sub>4</sub>-PEG and Fe<sub>3</sub>O<sub>4</sub>-PEG-Cy7-EMO from in vivo MRI images (Figure 6C). As is shown in Figure 6D, the signal intensity ratio ( $SIR = SI_{\text{tumor}} / SI_{\text{muscle}}$ ) trough was reached at 6 hours after the NPs were injected, and then the SIR gradually rose as time passed for Fe<sub>3</sub>O<sub>4</sub>-PEG-Cy7-EMO group. Similar trend of SIR was observed in Fe<sub>3</sub>O<sub>4</sub>-PEG group (Figure 6C and D).

To further verify the passive targeting ability of Fe<sub>3</sub>O<sub>4</sub>-PEG-Cy7-EMO, in vivo FI experiments were also done before and after the NPs were injected. Three mice were sacrificed at 6, 24, and 48 hours after the NPs were injected. As is shown in Figure 6E, the signals of NPs were mainly detected in liver at 2 hours after the NPs were injected. Then, the fluorescence signals were detected in tumor at 6, 24, and 48 hours after the NPs were injected. Interestingly, the fluorescence signals were also detected in kidneys at 24 and 48 hours after the NPs were injected, which may be attributed that the NPs were finally metabolized by the kidneys. From Figure 6F, we can see that the signals in liver decreased 2 hours after the NPs were injected. By contrast, the fluorescence intensity of the tumor remained steady even 48 hours after the NPs were injected.

Subsequently, the H&E staining (Figure 7A) and Prussian Blue staining (Figure 7B) were performed in the hearts, livers, spleens, lungs, kidneys, and pancreatic tumors. High levels of iron-positive cells were observed in the livers and pancreatic tumors, but few were observed in the hearts, spleens, lungs, and kidneys 48 h after injection of Fe<sub>3</sub>O<sub>4</sub>-PEG-Cy7-EMO (Figure 7B). Additionally, we also performed the H&E staining to examine the toxic effects of Fe<sub>3</sub>O<sub>4</sub>-PEG-Cy7-EMO on hearts, livers, spleens,

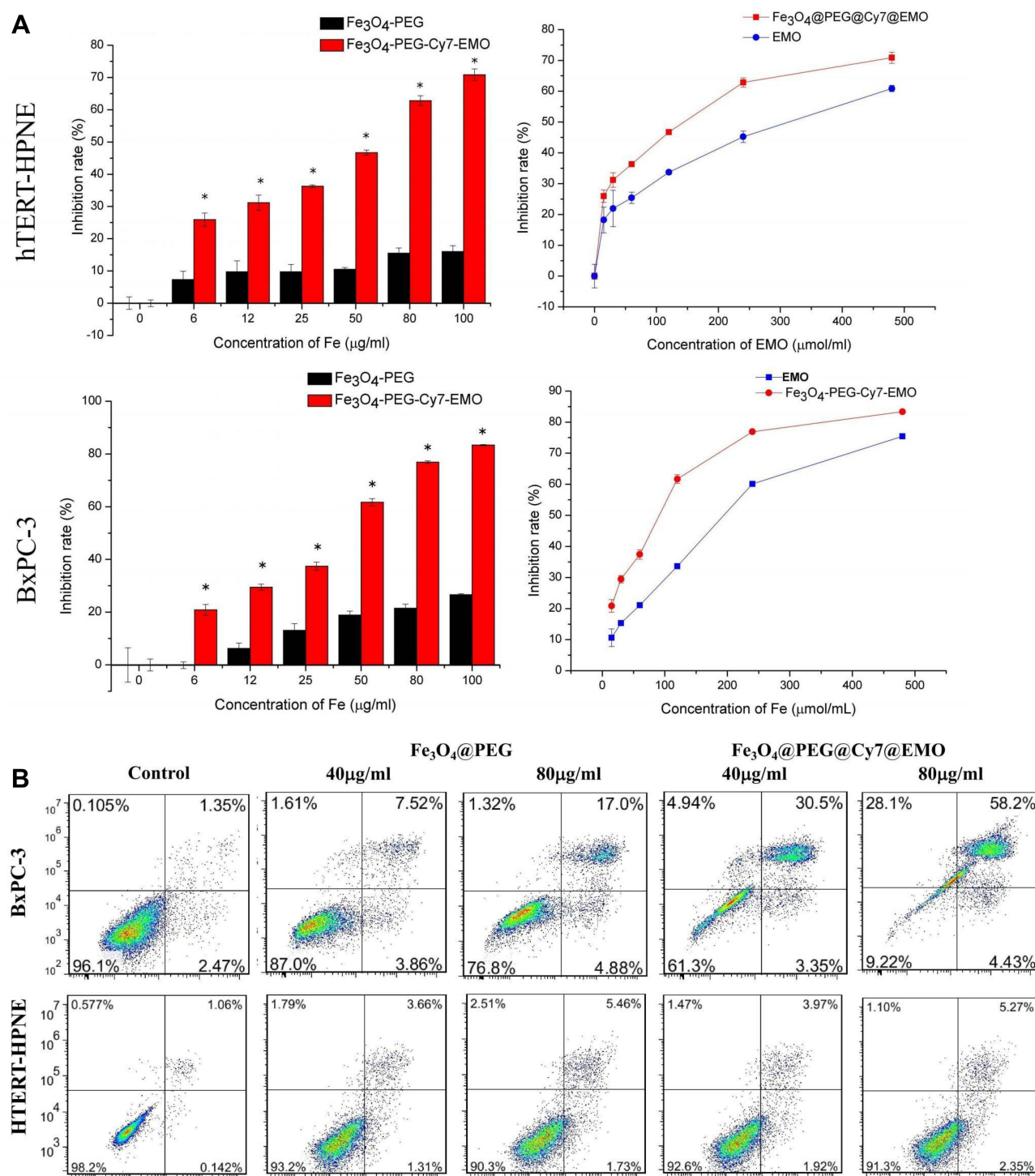


**Figure 5** (A) The MTT results of BxPC-3 and hTERT-HPNE cells incubated with  $\text{Fe}_3\text{O}_4$ -PEG,  $\text{Fe}_3\text{O}_4$ -PEG-Cy7-EMO, and EMO. (B) Apoptosis assays for BxPC-3 and hTERT-HPNE cells after different treatment. \* $P < 0.05$  for  $\text{Fe}_3\text{O}_4$ -PEG vs  $\text{Fe}_3\text{O}_4$ -PEG-Cy7-EMO.

lungs, and kidneys. As is shown in Figure 7A, there was no obvious damage to organs, indicating that the NPs can be used in vivo.

Finally, the in vivo antitumor efficacy of  $\text{Fe}_3\text{O}_4$ -PEG-Cy7-EMO was examined using orthotopic human

pancreatic tumor xenograft models, using  $\text{Fe}_3\text{O}_4$ -PEG, EMO, and saline as control groups. Figure 8A demonstrates the body weight changes of mice in different treatment groups, indicating no systemic toxic response in mice since the body weight increased over time. As is



**Table 1** The Apoptotic Rates of BxPC-3 and hTERT-HPNE Cells Incubated with Different Concentrations of NPs

Cell Lines	Control	Fe <sub>3</sub> O <sub>4</sub> -PEG (40μg/mL)	Fe <sub>3</sub> O <sub>4</sub> -PEG (80μg/mL)	Fe <sub>3</sub> O <sub>4</sub> -PEG-Cy7-EMO (40μg/mL)	Fe <sub>3</sub> O <sub>4</sub> -PEG-Cy7-EMO (80μg/mL)
BxPC-3	3.82%	11.38%	21.88%	33.85%	62.23%
hTERT-HPNE	1.20%	4.97%	7.19%	5.89%	7.62%

**Note:** Apoptotic rates = pre-apoptotic rate + post-apoptotic rate.

shown in Figure 8B, Fe<sub>3</sub>O<sub>4</sub>-PEG-Cy7-EMO had the most obvious inhibitory effect on tumor growth since tumor volume in this group was significantly smaller than

Fe<sub>3</sub>O<sub>4</sub>-PEG group and saline group. Tumors were harvested on day 14 for observation; as a result, tumor volume in Fe<sub>3</sub>O<sub>4</sub>-PEG-Cy7-EMO group was the smallest

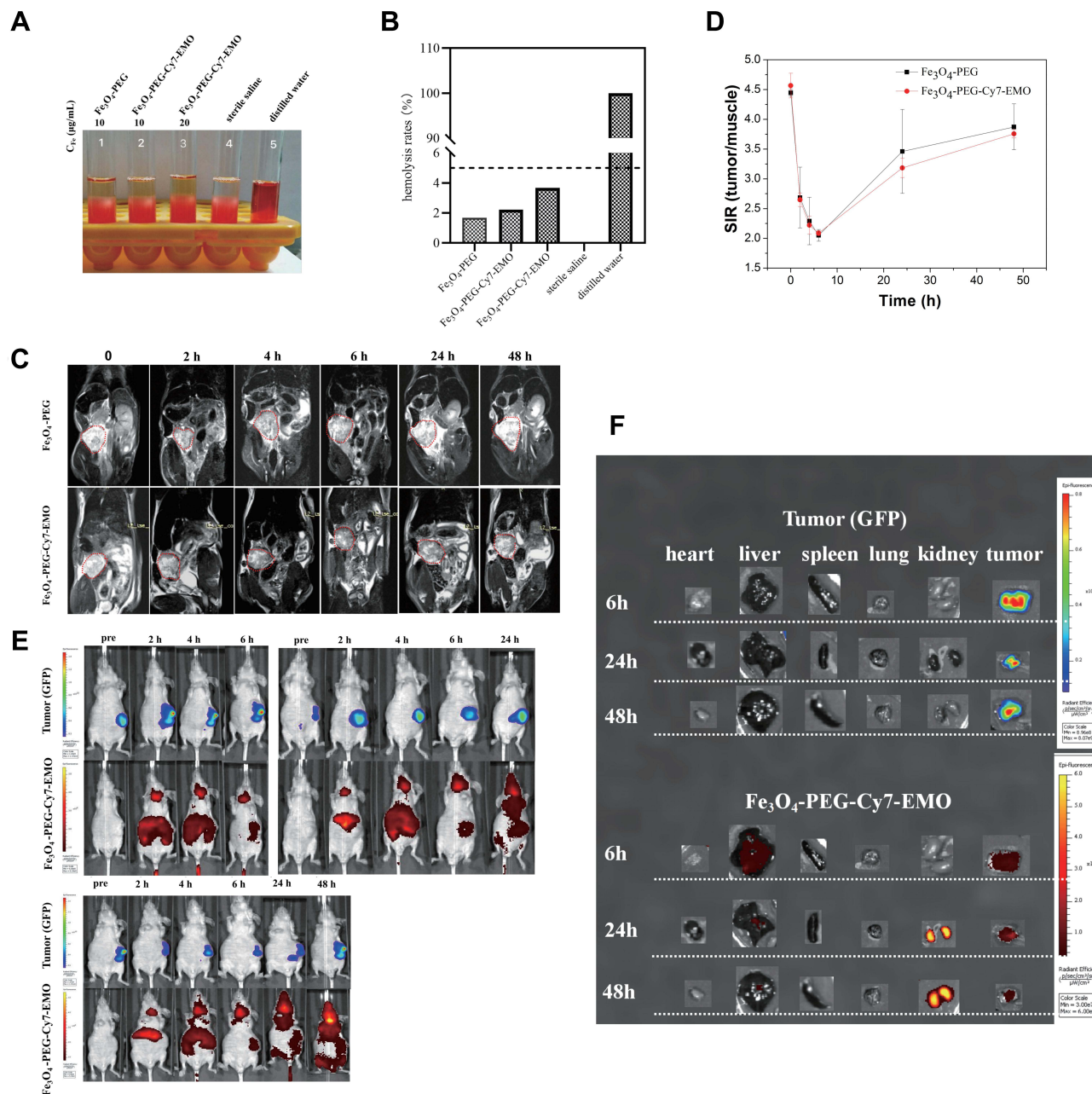


**Figure 6** (A) The hemolysis experiments in vitro. Different treatments of tubes 1–5 are clarified in (B). (C) In vivo MRI images and (D) time-dependent intensity curves of Fe<sub>3</sub>O<sub>4</sub>-PEG and Fe<sub>3</sub>O<sub>4</sub>-PEG-Cy7-EMO groups. (E) In vivo fluorescence imaging and (F) ex vivo fluorescence imaging of hearts, livers, spleens, lungs, and tumors.

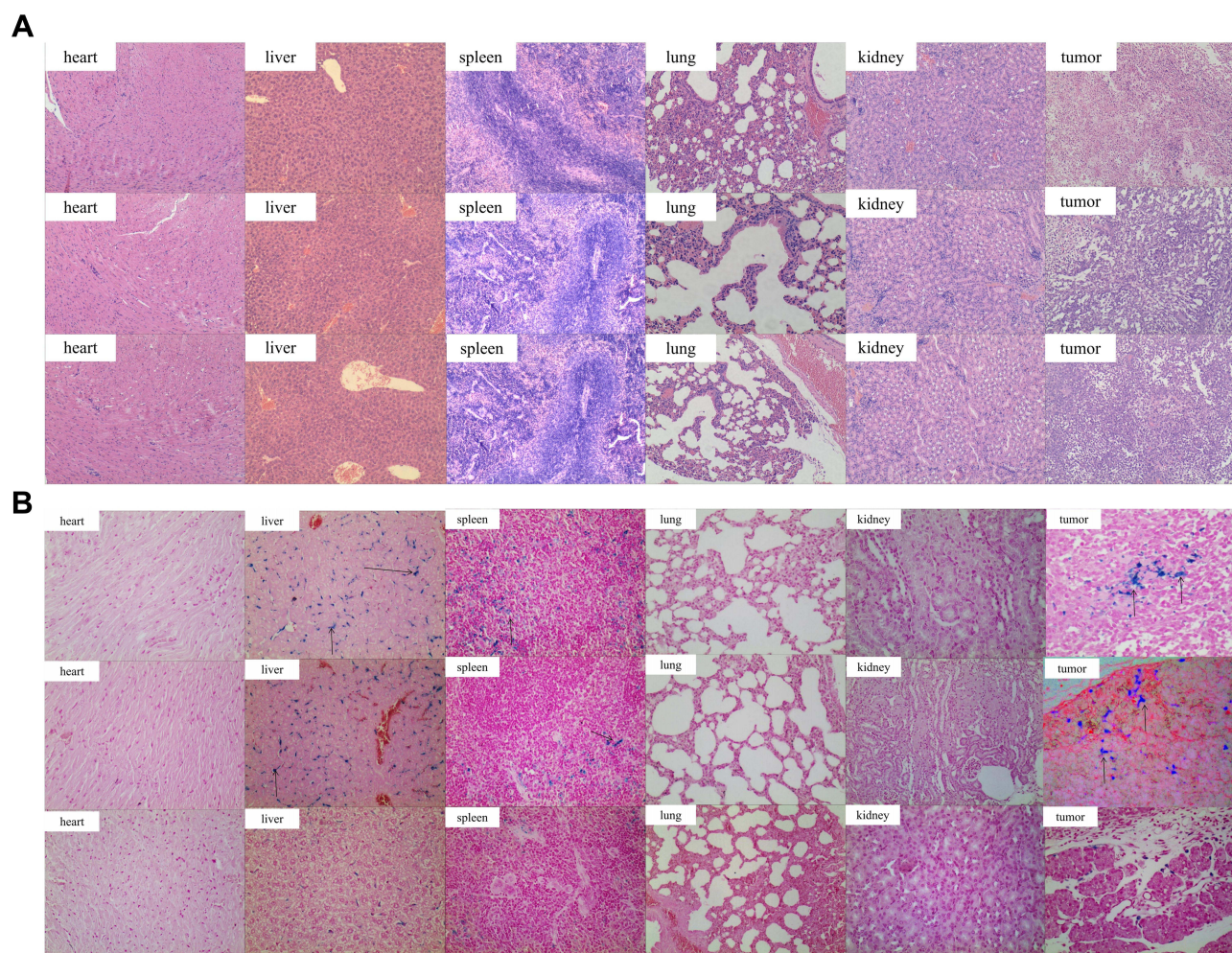


**Figure 7 (A)** The H&E staining of different organs including hearts, livers, spleens, lungs, and kidneys. No obvious pathological changes were observed. **(B)** Prussian Blue staining analyses of ex vivo.

(Figure 8C), which was in consistent with the assessment of tumor volume (Figure 8B).

## Discussion

Similar to normal tissue microenvironment, stromal, tumor, and immune cells and fibroblasts in tumor microenvironment (TME) are embedded in the extracellular matrix surrounded by blood vessels which provide oxygen and nutrient.<sup>39</sup> Notably, four unique features were identified in TME: 1) endothelial leakiness and discontinuity in the vasculature; 2) low pH; 3) poor oxygenation; 4) high interstitial pressure.<sup>40</sup> Considering the abovementioned differences, the EPR effect may occur by allowing selective targeting to TME.<sup>41–43</sup> EPR effect is one of the most widely used mechanisms for passive targeting of NPs to solid tumors. Obviously, leaky vasculature and the EPR effect might allow fractional accumulation of NPs in the

tumor tissue and consequently facilitate in fulfilled treatments.<sup>44,45</sup> To date, several passively targeted delivery systems including Doxil (1995), a liposomal delivery system of doxorubicin, Abraxane (2005), and a polymeric micelle delivery vehicle of paclitaxel, Genexol-PM (2007), have been approved by the FDA.<sup>46</sup> In this study, we successfully constructed EMO-loaded, Cy7-functionalized, PEG-coated  $\text{Fe}_3\text{O}_4$  ( $\text{Fe}_3\text{O}_4$ -PEG-Cy7-EMO).  $\text{Fe}_3\text{O}_4$ -PEG-Cy7-EMO NPs have several vital properties: stronger magnetic susceptibility effects, good biocompatibility, passively targeting of pancreatic cancer, potential for FI/MR imaging, drug loading and release behavior, few side effects, and high efficacy against tumors.

It is reported that there are two barriers NPs may encounter after intravenous administration:<sup>47</sup> 1) Protein corona is induced by the process that abundant blood



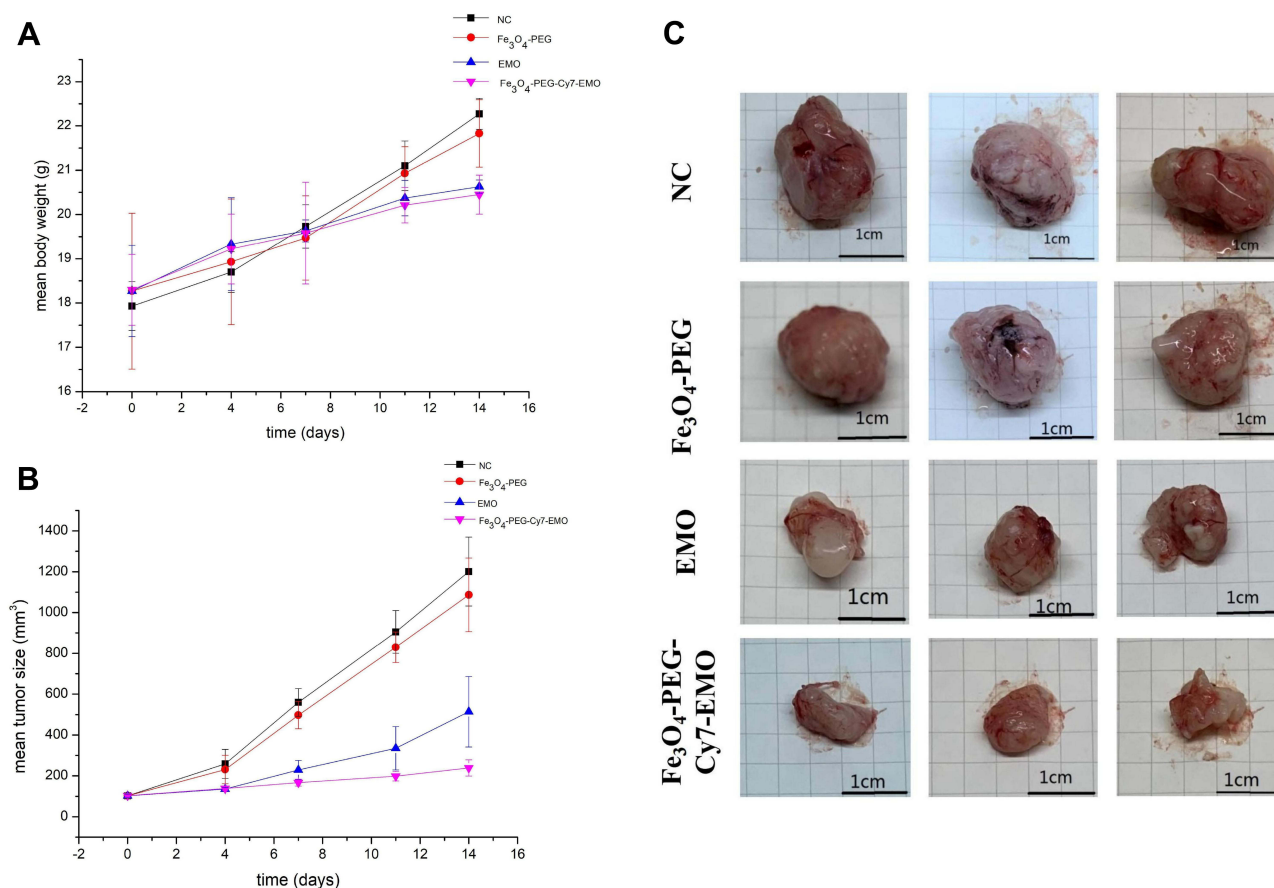


**Figure 8** In vivo anti-tumor efficiency.

**Notes:** (A) Body weight changes of BxPC-3 tumor-bearing nude mice in different treatment groups. (B) Tumor volume changes of BxPC-3 tumor-bearing nude mice in different treatment groups. (C) Photos of tumors after treatment using 0.9% saline, Fe<sub>3</sub>O<sub>4</sub>-PEG, EMO, and Fe<sub>3</sub>O<sub>4</sub>-PEG-Cy7-EMO after two weeks.

proteins including albumin and lipoproteins will absorb non-specifically on the NP surface. This process will influence the clearance process, alter the in vivo biodistribution and targeting efficiency; 2) The next barrier is to escape the blood vessels and accumulate at the target sites. EPR effect has facilitated in the extravasation of NPs into the TME, and many efforts have been made to optimize the size, shape, and electrical charge for passive tumor delivery and targeting. In the present study, the hydrodynamic sizes of Fe<sub>3</sub>O<sub>4</sub>-PEG and Fe<sub>3</sub>O<sub>4</sub>-PEG-Cy7-EMO were  $9.1 \pm 1.7$  nm and  $9.9 \pm 1.2$  nm, which allowed them to accumulate at the tumor site. The potential of NPs is affected by their property of nonspecific binding of proteins.<sup>48</sup> As compared to positively charged NPs, negatively charged NPs have a lower frequency to bind to plasma proteins; high protein binding will result in more rapid clearance of NPs by Kupffer cells.<sup>49</sup> The zeta potentials of Fe<sub>3</sub>O<sub>4</sub>-PEG and Fe<sub>3</sub>O<sub>4</sub>-PEG-Cy7-EMO were  $-40.2 \pm 6.83$  mV and  $-38.7 \pm 6.32$  mV, which had optimal potentials and were suitable for in vivo applications.

Additionally, further experiments were carried out to prove the stability of the NPs since they were stable in sodium chloride (0 to 1.0 mM) solution (containing 5% BSA) and in different pH (3 to 11) solution.

Subsequently, the cellular uptake of Fe<sub>3</sub>O<sub>4</sub>-PEG-Cy7-EMO in BxPC-3 and hTERT-HPNE cells was assessed using a bio-TEM and Prussian blue staining. The bio-TEM results showed that a higher frequency of Fe<sub>3</sub>O<sub>4</sub>-PEG-Cy7-EMO NPs were observed in BxPC-3 cells than in hTERT-HPNE cells, which were trapped in lysosomes and endosomes. These results were consistent with the results obtained by Prussian Blue staining analysis. MTT assay and flow cytometry assay results showed remarkable therapeutic effects of Fe<sub>3</sub>O<sub>4</sub>-PEG-Cy7-EMO in BxPC-3 cells compared to hTERT-HPNE cells, which could be explained by the fact that PC cells have a stronger phagocytic ability than normal pancreatic cells.

The hemolysis experiment indicated that the NPs have good biocompatibility and are suitable for further in vivo experiments. It is reported that FI has high

detection sensitivity, but the spatial resolution is low.<sup>5,50</sup> However, the anatomical resolution of MRI is high, but the sensitivity is low.<sup>51,52</sup> In the present study, we assembled the Fe<sub>3</sub>O<sub>4</sub>-PEG-Cy7-EMO for a combination of FI and MRI. In vivo MRI experiments showed the time-dependent biodistribution of NPs. The SIR trough was reached at 6 hours after the NPs were injected, and then the SIR gradually rose as time passed. In vivo FI experiments also showed the biodistribution of NPs in tumors, which were observed at 6, 24, and 48 hours after injection. Additionally, the fluorescence signals were also detected in kidneys at 24 and 48 hours after the NPs were injected, which may be explained by the fact that the NPs were finally metabolized by kidneys. Fe<sub>3</sub>O<sub>4</sub>-PEG-Cy7-EMO combines the advantages of FI and MRI in one platform with higher sensitivity and resolution, which can provide useful information in PC diagnosis.

Histological analysis was performed to investigate the toxicity of Fe<sub>3</sub>O<sub>4</sub>-PEG-Cy7-EMO in vivo. No obvious pathological changes were observed in hearts, livers, spleens, lungs, and kidneys, indicating that the NPs can be used in vivo experiments. Subsequently, the Prussian Blue staining experiments showed high levels of iron-positive cells in the livers and pancreatic tumors, but few in the hearts, spleens, lungs, and kidneys 48 h after injection of Fe<sub>3</sub>O<sub>4</sub>-PEG-Cy7-EMO. Antitumor experiments were subsequently performed to investigate the acute toxicity of Fe<sub>3</sub>O<sub>4</sub>-PEG-Cy7-EMO in vivo, which had the most obvious inhibitory effect on tumor growth since tumor volume in this group was significantly smaller than Fe<sub>3</sub>O<sub>4</sub>-PEG group and saline group.

There were several limitations in this study. First, we assembled a passive-targeted emodin-conjugated PEGylation of Fe<sub>3</sub>O<sub>4</sub> NPs for FI/MRI dual-modal imaging and therapy in pancreatic cancer. Though the NPs demonstrate the potentials in FI/MRI imaging and therapy of pancreatic cancer, the performances as targeted probes in pancreatic cancer are still unclear. Second, further research is needed to investigate the efficiency when this kind of NPs candidates in conjugation with specific targeting ligands as per the affinity for highly expressed proteins by certain tumors for active-targeting approach. Third, the tumors reached 5–10 mm in diameter in the present study; however, it is not clear if these tumors are at an early stage. Fourth, NIR imaging might not be suitable for patients with pancreatic cancer due to the penetration depth. Fifth, many NPs were trapped by the mononuclear phagocyte system in livers, how to make the NPs evade immune

surveillance and penetrate into the tumor tissue is pivotal to maximize the therapeutic potency, but it is challenging.<sup>53</sup>

In conclusion, we established a new multifunctional nanoplatform designated Fe<sub>3</sub>O<sub>4</sub>-PEG-Cy7-EMO providing FI/MRI imaging and therapeutic treatment for PC cells. In vivo FI and MRI experiments showed the passive targeting and contrast ability of the nanoprobes in tumor-bearing mouse models. Utilization of this nanoplatform enables the detection and therapy of early-stage pancreatic cancer.

## IRB Statement

All animal experiments were performed in compliance with the ethical guidelines established by the local animal care authorities at Affiliated Hospital of Nanjing University of Chinese Medicine (2019 DW-19-02).

## Acknowledgments

This study was supported by the Administration of Traditional Chinese Medicine of Jiangsu Province (No. ZD201907) and National Natural Science Foundation of China (81901797, 81771899).

## Disclosure

The authors report no conflicts of interest concerning this article.

## References

1. Siegel RL, Miller KD, Fuchs HE, et al. Cancer statistics, 2021. *CA Cancer J Clin*. 2021;71(1):7–33. doi:10.3322/caac.21654
2. Kulkarni NM, Mannelli L, Zins M, et al. White paper on pancreatic ductal adenocarcinoma from society of abdominal radiology's disease-focused panel for pancreatic ductal adenocarcinoma: part II, update on imaging techniques and screening of pancreatic cancer in high-risk individuals. *Abdom Radiol*. 2020;45(3):729–742. doi:10.1007/s00261-019-02290-y
3. Kulkarni NM, Soloff EV, Tolat PP, et al. White paper on pancreatic ductal adenocarcinoma from society of abdominal radiology's disease-focused panel for pancreatic ductal adenocarcinoma: part I, AJCC staging system, NCCN guidelines, and borderline resectable disease. *Abdom Radiol*. 2020;45(3):716–728. doi:10.1007/s00261-019-02289-5
4. Rahib L, Smith BD, Aizenberg R, Rosenzweig AB, Fleshman JM, Matrisian LM. Projecting cancer incidence and deaths to 2030: the unexpected burden of thyroid, liver, and pancreas cancers in the United States. *Cancer Res*. 2014;74(11):2913–2921. doi:10.1158/0008-5472.CAN-14-0155
5. Huang X, Fan C, Zhu H, et al. Glypican-1-antibody-conjugated Gd–Au nanoclusters for FI/MRI dual-modal targeted detection of pancreatic cancer. *Int J Nanomedicine*. 2018;13:2585–2599. doi:10.2147/IJN.S158559
6. Qiu W, Chen R, Chen X, et al. Oridonin-loaded and GPC1-targeted gold nanoparticles for multimodal imaging and therapy in pancreatic cancer. *Int J Nanomedicine*. 2018;13:6809–6827. doi:10.2147/IJN.S177993
7. Akhter MH, Kumar S, Nomani S. Sonication tailored enhance cytotoxicity of naringenin nanoparticle in pancreatic cancer: design, optimization, and in vitro studies. *Drug Dev Ind Pharm*. 2020;46(4):659–672. doi:10.1080/03639045.2020.1747485

8. Tummers WS, Willmann JK, Bonsing BA, Vahrmeijer AL, Gambhir SS, Swijnenburg RJ. Advances in diagnostic and intraoperative molecular imaging of pancreatic cancer. *Pancreas*. 2018;47(6):675–689. doi:10.1097/MPA.0000000000001075
9. Singhi AD, Koay EJ, Chari ST, Maitra A. Early detection of pancreatic cancer: opportunities and challenges. *Gastroenterology*. 2019;156(7):2024–2040. doi:10.1053/j.gastro.2019.01.259
10. Israel LL. A nanomedicine approach to manage cancer – imaging pancreatic cancer using targeted iron oxide nanoparticles. *EBioMedicine*. 2018;30:7–8. doi:10.1016/j.ebiom.2018.03.011
11. Lin L, Fan Y, Gao F, et al. UTMD-promoted co-delivery of gemcitabine and miR-21 inhibitor by dendrimer-entrapped gold nanoparticles for pancreatic cancer therapy. *Theranostics*. 2018;8(7):1923–1939. doi:10.7150/thno.22834
12. Ma X, Wang S, Hu L, et al. Imaging characteristics of USPIO nanoparticles (<5 nm) as MR contrast agent in vitro and in the liver of rats. *Contrast Media Mol Imaging*. 2019;2019:3687537. doi:10.1155/2019/3687537
13. Chen X, Zhou H, Li X, et al. Plectin-1 targeted dual-modality nanoparticles for pancreatic cancer imaging. *EBioMedicine*. 2018;30:129–137. doi:10.1016/j.ebiom.2018.03.008
14. Khan S, Setua S, Kumari S, et al. Superparamagnetic iron oxide nanoparticles of curcumin enhance gemcitabine therapeutic response in pancreatic cancer. *Biomaterials*. 2019;208:83–97. doi:10.1016/j.biomaterials.2019.04.005
15. Xie W, Guo Z, Gao F, et al. Shape-, size-and structure-controlled synthesis and biocompatibility of iron oxide nanoparticles for magnetic theranostics. *Theranostics*. 2018;8(12):3284–3307. doi:10.7150/thno.25220
16. Song L, Zang F, Song M, Chen G, Zhang Y, Gu N. Effective PEGylation of Fe<sub>3</sub>O<sub>4</sub> nanomicelles for in vivo MR imaging. *J Nanosci Nanotechnol*. 2015;15(6):4111–4118. doi:10.1166/jnn.2015.9803
17. Patsula V, Horák D, Kučka J, et al. Synthesis and modification of uniform PEG-nitridonate-modified magnetic nanoparticles determines prolonged blood circulation and biodistribution in a mouse preclinical model. *Sci Rep*. 2019;9(1):10765. doi:10.1038/s41598-019-47262-w
18. Qie Y, Yuan H, Von Roemeling CA, et al. Surface modification of nanoparticles enables selective evasion of phagocytic clearance by distinct macrophage phenotypes. *Sci Rep*. 2016;6(1):26269. doi:10.1038/srep26269
19. Ahmad J, Ahmad MZ, Akhter H. Surface-engineered cancer nanomedicine: rational design and recent progress. *Curr Pharm Des*. 2020;26(11):1181–1190. doi:10.2174/1381612826666200214110645
20. Akhter MH, Beg S, Tarique M, et al. Receptor-based targeting of engineered nanocarrier against solid tumors: recent progress and challenges ahead. *Biochim Biophys Acta Gen Subj*. 2021;1865(2):129777. doi:10.1016/j.bbagen.2020.129777
21. Habban akhter M, Sateesh Madhav N, Ahmad J. Epidermal growth factor receptor based active targeting: a paradigm shift towards advance tumor therapy. *Artif Cells Nanomed Biotechnol*. 2018;46(sup 2):1188–1198. doi:10.1080/21691401.2018.1481863
22. Akhter MH, Rizwanullah M, Ahmad J, Ahsan MJ, Mujtaba MA, Amin S. Nanocarriers in advanced drug targeting: setting novel paradigm in cancer therapeutics. *Artif Cells Nanomed Biotechnol*. 2018;46(5):873–884. doi:10.1080/21691401.2017.1366333
23. Akhter MH, Amin S. An investigative approach to treatment modalities for squamous cell carcinoma of skin. *Curr Drug Deliv*. 2017;14(5):597–612. doi:10.2174/1567201801666160906104254
24. Wang Z, Chen H, Chen J, et al. Emodin sensitizes human pancreatic cancer cells to egfr inhibitor through suppressing stat3 signaling pathway. *Cancer Manag Res*. 2019;11:8463–8473. doi:10.2147/CMAR.S221877
25. Liu DL, Bu H, Li H, et al. Emodin reverses gemcitabine resistance in pancreatic cancer cells via the mitochondrial apoptosis pathway in vitro. *Int J Oncol*. 2012;40(4):1049–1057. doi:10.3892/ijo.2011.1285
26. Dai G, Ding K, Cao Q, et al. Emodin suppresses growth and invasion of colorectal cancer cells by inhibiting VEGFR2. *Eur J Pharmacol*. 2019;859:172525. doi:10.1016/j.ejphar.2019.172525
27. Ma W, Liu F, Yuan L, Zhao C, Chen C. Emodin and AZT synergistically inhibit the proliferation and induce the apoptosis of leukemia K562 cells through the EGR1 and the Wnt/ $\beta$ -catenin pathway. *Oncol Rep*. 2020;43(1):260–269. doi:10.3892/or.2019.7408
28. Song M, Zhang Y, Hu S, et al. Influence of morphology and surface exchange reaction on magnetic properties of monodisperse magnetite nanoparticles. *Colloids Surfaces A Physicochem Eng Asp*. 2012;408:114–121. doi:10.1016/j.colsurfa.2012.05.039
29. Mero A, Campisi M. Hyaluronic acid bioconjugates for the delivery of bioactive molecules. *Polymers*. 2014;6(1):346–369. doi:10.1021/bm400612h
30. Qiu W, Zhang H, Chen X, et al. A GPC1-targeted and gemcitabine-loaded biocompatible nanopatform for pancreatic cancer multimodal imaging and therapy. *Nanomedicine*. 2019;14(17):2339–2353. doi:10.2217/nnm-2019-0063
31. Jin L, Wang Q, Chen J, Wang Z, Xin H, Zhang D. Efficient delivery of therapeutic siRNA by Fe<sub>3</sub>O<sub>4</sub> magnetic nanoparticles into oral cancer cells. *Pharmaceutics*. 2019;11(11):615. doi:10.3390/pharmaceutics11110615
32. Syed Abdul Rahman SN, Abdul Wahab N, Abd Malek SN. In vitro morphological assessment of apoptosis induced by antiproliferative constituents from the rhizomes of curcuma zedoaria. *Evid Based Complement Alternat Med*. 2013;2013:257108. doi:10.1155/2013/257108
33. Guo L, Chen B, Liu R, et al. Biocompatibility assessment of poly-ethylene glycol-poly L-lysine-poly lactic-co-glycolic acid nanoparticles in vitro and in vivo. *J Nanosci Nanotechnol*. 2015;15(5):3710–3719. doi:10.1166/jnn.2015.9509
34. Seyfert UT, Biehl V, Schenk J. In vitro hemocompatibility testing of biomaterials according to the ISO 10993-4. *Biomol Eng*. 2002;19(2–6):91–96. doi:10.1016/s1389-0344(02)00015-1
35. Lwin TM, Murakami T, Miyake K, et al. Tumor-specific labeling of pancreatic cancer using a humanized anti-CEA antibody conjugated to a near-infrared fluorophore. *Ann Surg Oncol*. 2018;25(4):1079–1085. doi:10.1245/s10434-018-6344-6
36. Hinton JP, Dvorak K, Roberts E, et al. A method to reuse archived H&E stained histology slides for a multiplex protein biomarker analysis. *Methods Protoc*. 2019;2(4):86. doi:10.3390/mps2040086
37. Liu B, Wang W, Fan J, et al. RBC membrane camouflaged Prussian blue nanoparticles for gambutolin loading and combined chemo/photothermal therapy of breast cancer. *Biomaterials*. 2019;217:119301. doi:10.1016/j.biomaterials.2019.119301
38. Jing L, Liang X, Deng Z, et al. Prussian blue coated gold nanoparticles for simultaneous photoacoustic/CT bimodal imaging and photothermal ablation of cancer. *Biomaterials*. 2014;35(22):5814–5821. doi:10.1016/j.biomaterials.2014.04.005
39. Spill F, Reynolds DS, Kamm RD, Zaman MH. Impact of the physical microenvironment on tumor progression and metastasis. *Curr Opin Biotechnol*. 2016;40:41–48. doi:10.1016/j.copbio.2016.02.007
40. Cairns R, Papandreou I, Denko N. Overcoming physiologic barriers to cancer treatment by molecularly targeting the tumor microenvironment. *Mol Cancer Res*. 2006;4(2):61–70. doi:10.1158/1541-7786.MCR-06-0002
41. Iyer AK, Khaled G, Fang J, Maeda H. Exploiting the enhanced permeability and retention effect for tumor targeting. *Drug Discov Today*. 2006;11(17–18):812–818. doi:10.1016/j.drudis.2006.07.005
42. Maeda H. Macromolecular therapeutics in cancer treatment: the EPR effect and beyond. *J Control Release*. 2012;164(2):138–144. doi:10.1016/j.jconrel.2012.04.038
43. Akhter MH, Rizwanullah M, Ahmad J, et al. Molecular targets and nanoparticulate systems designed for the improved therapeutic intervention in Glioblastoma Multiforme. *Drug Res*. 2021;71(3):122–137. doi:10.1055/a-1296-7870

44. Chrastina A, Massey KA, Schnitzer JE. Overcoming in vivo barriers to targeted nanodelivery. *Wiley Interdiscip Rev Nanomed Nanobiotechnol.* **2011**;3(4):421–437. doi:10.1002/wnan.143
45. Tang Y, Soroush F, Sheffield JB, Wang B, Prabhakarandian B, Kiani MF. A biomimetic microfluidic tumor microenvironment platform mimicking the EPR effect for rapid screening of drug delivery systems. *Sci Rep.* **2017**;7(1):9359. doi:10.1038/s41598-017-09815-9
46. Clemons TD, Singh R, Sorolla A, Chaudhari N, Hubbard A, Iyer KS. Distinction between active and passive targeting of nanoparticles dictate their overall therapeutic efficacy. *Langmuir.* **2018**;34(50):15343–15349. doi:10.1021/acs.langmuir.8b02946
47. Pandit S, Dutta D, Nie S. Active transcytosis and new opportunities for cancer nanomedicine. *Nat Mater.* **2020**;19(5):478–480. doi:10.1038/s41563-020-0672-1
48. Chao Y, Karmali PP, Mukthavaram R, et al. Direct recognition of superparamagnetic nanocrystals by macrophage Scavenger Receptor SR-AI. *ACS Nano.* **2013**;7(5):4289–4298. doi:10.1021/nn400769e
49. Pelegri-O'Day EM, Lin EW, Maynard HD. Therapeutic protein-polymer conjugates: advancing beyond PEGylation. *J Am Chem Soc.* **2014**;136(41):14323–14332. doi:10.1021/ja504390x
50. Xu C, Wang Y, Zhang C, Jia Y, Luo Y, Gao X. AuGd integrated nanopores for optical/MRI/CT triple-modal in vivo tumor imaging. *Nanoscale.* **2017**;9(13):4620–4628. doi:10.1039/c7nr01064h
51. Li Y, Guo W, Su X, et al. Facile preparation of near-infrared fluorescence and magnetic resonance dual-modality imaging probes based on mesoporous organosilica nanoparticles. *J Colloid Interface Sci.* **2019**;539:277–286. doi:10.1016/j.jcis.2018.12.067
52. Kyeong S, Kim J, Chang H, et al. Magnetic nanoparticles. *Adv Exp Med Biol.* **2021**;1309:191–215. doi:10.1007/978-981-33-6158-4\_8
53. Xu Z, Huang H, Xiong X, et al. A near-infrared light-responsive extracellular vesicle as a “Trojan horse” for tumor deep penetration and imaging-guided therapy. *Biomaterials.* **2021**;269:120647. doi:10.1016/j.biomaterials.2020.120647

## International Journal of Nanomedicine

Dovepress

### Publish your work in this journal

The International Journal of Nanomedicine is an international, peer-reviewed journal focusing on the application of nanotechnology in diagnostics, therapeutics, and drug delivery systems throughout the biomedical field. This journal is indexed on PubMed Central, MedLine, CAS, SciSearch®, Current Contents®/Clinical Medicine,

Journal Citation Reports/Science Edition, EMBase, Scopus and the Elsevier Bibliographic databases. The manuscript management system is completely online and includes a very quick and fair peer-review system, which is all easy to use. Visit <http://www.dovepress.com/testimonials.php> to read real quotes from published authors.

Submit your manuscript here: <https://www.dovepress.com/international-journal-of-nanomedicine-journal>